International Journal of Solids and Structures 171 (2019) 81–91

Contents lists available at ScienceDirect

International Journal of Solids and Structures

journal homepage: www.elsevier.com/locate/ijsolstr

An analytical model for the flat punch indentation size effect

C.J. Campbell, S.P.A. Gill*

Department of Engineering, University of Leicester, University Road, Leicester LE1 7RH, UK

ARTICLE INFO

Article history:
Received 28 November 2018
Revised 3 April 2019
Available online 5 May 2019

Keywords:
Size effects
Indentation
Flat punch
Analytical model

ABSTRACT

An analytical approximation for the indentation size effect (ISE) due to plane strain flat punch nanoindentation is derived. The flat punch ISE differs from that observed for self-similar (pointed) and spherical indenters in a number of ways: (1) the contact area does not change; (2) the contact pressure depends on two length scales not just one (the punch width and the indentation depth); (3) the profile of the punch is not differentially continuous, resulting in singular plastic strain gradients at the sharp edges, such that (4) the shape and connectivity of the plastic zones change with indentation depth and punch width, resulting in (5) changes in the proportion of the deformation accommodated by elasticity and plasticity are important, meaning that a fully elastoplastic model is required. Complete loading-unloading curves are modelled, with the calibration of geometrical parameters from finite element strain gradient plasticity simulations. As the punch width decreases, it is observed that there are increases in the indentation pressure, the relative size of the plastic zone(s) and the elastic component of the deformation. These predictions are found to compare favourably with experimental measurements in the literature. The model is extended to incorporate the consequence of imposing natural limitations on the maximum dislocation density at the edges. It is suggested that observable changes in the plastic zone morphology with the ISE make this an experimentally interesting area for the validation of size effects in plasticity.

1. Introduction

The indentation size effect (ISE) is an experimentally observed phenomenon in which the measured hardness of a material is found to increase as the size of the indent decreases. Nix and Gao (1998) first proposed a model to explain this behaviour based on forest hardening due to the presence of the geometrically necessary dislocations (GNDs) that are required to accommodate plastic strain gradients in a crystal. The current analysis is based on this approach whereby the shear yield stress is assumed to be

$$\tau_Y = \beta_F G b \sqrt{\rho} \tag{1}$$

where G is the shear modulus of the material, $b = 0.25$ nm is the magnitude of the Burgers vector, and β_F is a dimensionless parameter which represents the strengthening contribution of dislocations from forest hardening. The total dislocation density, $\rho = \rho_S + \rho_G$, is assumed to be the sum of a constant pre-existing statistically-stored dislocation (SSD) population of density ρ_S, and that due to a locally evolving population of GNDs, ρ_G, derived from the plastic strain gradient. The size-dependent hardness of the material is then expressed as

$$H = 3\sqrt{3}\tau_Y = H_0\sqrt{1 + \frac{\rho_G}{\rho_S}} \tag{2}$$

where $H_0 = 3\sqrt{3}\beta_F G b \sqrt{\rho_S}$ is the macroscopic hardness (at which $\rho_G \to 0$). GNDs are required to form the numerous surface steps of height b that define the shape of the plastic indent. For spherical and self-similar indenters, the number of surface steps (and hence GNDs) are readily determined from the slope of the indenter profile if the contribution from elastic deformation is ignored. A central assumption of the Nix and Gao (1998) model is that the volume they occupy (the plastic zone) is a hemispherical region below the indenter, and that the radius, c, of this region is the (plastic) contact radius.

Nix and Gao (1998) derived the hardness size effect for a self-similar (pointed) indenter. Assuming a conical shape with angle θ to the horizontal, the resulting GND density (total length of surface steps divided by plastic zone volume) is found to be $\rho_G = \frac{3tan\theta}{2cb}$. Eq. (2) then gives the standard expression

$$H = H_0\sqrt{1 + \frac{h^*}{h}} \tag{3}$$

where h is the indentation depth, such that $tan\theta = \frac{h}{c}$, and $h^* = \frac{3\tan^2\theta}{2b\rho_S}$ is a material length scale (Nix and Gao, 1998).

* Corresponding author.
E-mail address: spg3@leicester.ac.uk (S.P.A. Gill).

https://doi.org/10.1016/j.ijsolstr.2019.05.004
0020-7683/

This analysis was later extended to spherical indenters by Swadener et al. (2002). This predicts an entirely different scaling behaviour. For a spherical indenter of radius R, the GND density $\rho_G = \frac{1}{bR}$ is independent of the indentation depth, such that Eq. (2) becomes

$$H = H_0\sqrt{1 + \frac{R^*}{R}} \tag{4}$$

where in this case $R^* = \frac{1}{b\rho_S}$ is the material length scale (Swadener et al., 2002).

However flat punch indentation differs significantly from both the spherical and the self-similar cases. Firstly, the indentation area does not change, so that the standard definition of hardness (force over indentation area) does not technically apply as the force changes without the area changing. Hence we refer to the average indentation pressure, P, in relation to the flat punch tests rather than hardness, H. The second difference is that the conceptual model of surface steps generated on the substrate surface due to the plastic deformation breaks down, as such steps would no longer be distributed smoothly across the contact area, as is the case with an indenter with a finite profile slope. A flat punch profile has zero slope under the indenter and an infinite slope at the edges. Therefore, within the conceptualisation of the Nix–Gao approach and perfect plasticity, the equivalent flat punch model would propose a single plastic surface step at the punch edges, with a height equivalent to the indentation depth δ, from which a very large number of GNDs ($\frac{\delta}{b}$) would be injected from this single point into the substrate. This is not the case, due to significant load transfer, and hence a different approach must be taken. In practice, plasticity will start at the punch edges, and the plastic zone will expand outwards from these sharp features, increasing in size with the indentation depth. This will happen due to the nature of the stress field under the indenter, even without local hardening. Surface steps, and GNDs, will be created under the flat punch indenter even though the indenter profile is flat. This is because both the elastic and plastic components of the deformation under the indenter must be considered. Upon unloading, the non-uniform plastic surface profile of the substrate underneath the flat punch can be clearly seen. These surface steps must be accommodated by GNDs. The third difference from the Nix–Gao model is that, as already observed, the size of the plastic zone changes but the contact radius does not. Consequently, unlike the spherical and self-similar indenter cases, there is no simple geometrical method for estimating the number of GNDs required to accommodate the shape of the plastic indentation, or for estimating the size of the plastic zone. It will prove to be necessary to consider the elastic deformation as well as the plastic deformation to develop a simple analytical model for the ISE which is equivalent to Eqs. (3) and (4) derived for the spherical and self-similar indenters. For spherical indentation (4) shows that the dominant ISE length scale is the size of the indenter, whereas for self-similar indenters, Eq. (3) shows that it is the indentation depth. We will show that, for a flat punch indenter, the indentation pressure depends on both the indenter size (width) and indentation depth.

Chen et al. (2010) have investigated the flat punch ISE experimentally in single crystal aluminium. They proposed that, for a flat punch of width $2a$, the average indentation pressure might vary through a relationship that is similar in form to (3) and (4) such that

$$P = P_0\sqrt{1 + \frac{a^*}{a}} \tag{5}$$

where P_0 is the macroscopic indentation pressure and a^* is a fitting constant for the ISE. This assumes that the indentation depth is a fixed fraction of the punch width. Eq. (5) is shown to fit their experimental results reasonably well over the fairly narrow range of punch widths considered (from 0.55 to 5 μm). However, it will be shown that this empirical model is not generally valid across a wide range of length scales.

Flat punches are also of interest for their use in microforming processes. Microscale devices fabricated from metals have been shown to perform better than silicon based devices, or are capable of performing functions which those manufactured from silicon cannot (Jiang et al., 2006). The understanding of mechanical interactions which occur during the micro-moulding of these metals is, therefore, of considerable significance. One important technique used for manufacturing of metal based HARMS (High-aspect-ratio microscale structures) is the LiGA (Lithographie Glavanoformung Abformung) process, which is reliant on electrodeposition, X-ray lithography, and moulding. LiGA is a fairly slow and expensive processes, so improving the moulding stage is of considerable importance in making it more economical for the production of HARMS (Cao et al., 2004; Meng et al., 2004). During the LiGA process there can be unexpected or unwanted structural changes in the material being moulded as well as changes in the yield strength (Cho et al., 2003); a better understanding of how the flat punch and material interact can help to improve the final material strength and hardness. Other applications of flat punches include the roll moulding of microchannels and fretting fatigue experiments (Ciavarella et al., 1998; Lu and Meng, 2014). Meng et al. (2004) have investigated the contact pressures occurring during the micro-moulding process for very large indentation depths, which are 2 or 3 times the width of the indenter. The normalised moulding stress prediction showed good correlation when compared to their experimental data for full plasticity for very deep indentations.

It is worth noting that the effect of punch misalignment is not considered here. Experimental (Pelletier et al., 2007) and numerical studies based on elastic analysis (Gourgiotis et al., 2016) and elastoplastic analysis for both conical indenters (Xu and Li, 2007) and cylindrical flat punches (Shahjahan and Hu, 2016) demonstrate that this can have a significant effect during the early stages of indentation, although the effect is less noticeable once extensive plasticity has been induced. Exact alignment for flat punch indentation can be challenging, with tools proposed to achieve good alignment (Pelletier et al., 2007). An alternative approach would be to place relatively thick, flat stiff disks or plates on the substrate. These would be naturally self-aligning and could be punched into the substrate using a larger radius spherical indenter.

Nielsen et al. (2014) have conducted numerical strain gradient plasticity simulations using the Fleck-Hutchinson plasticity model to investigate the effect of size on the fabrication of microscale features in metals. They also considered the effect of friction in determining the final profile of the resulting indent. This deviates significantly from the macroscale indent due to the enhanced level of elastic recovery at smaller scales. Guha et al. (2014) have also simulated flat punch indentation from the perspective of a moulding technique using a modified Fleck-Hutchinson plasticity model. For both approaches, the origin of a size hardening effect is clearly demonstrated over a fairly small range of punch sizes, typically one order of magnitude or less. In this paper, the flat punch ISE is investigated across many orders of magnitude and an analytic expression for the loading and unloading response is derived. The analytical model is validated and calibrated against finite element simulations and the experimental results of Chen et al. (2010). The finite element model is introduced in Section 2. Firstly, its predictions for spherical and self-similar indenters compared with those from the Nix–Gao type models (3) and (4). The simulation is then utilised to determine the contact pressure vs displacement response for flat punch indenters of different widths. The analytical model is derived in Section 3 and its predictions are compared with the finite element results and experimental observations.

Further issues are explored in Section 4, where the sensitivity of the results to the plasticity model and other assumptions within the Nix–Gao approach are investigated.

2. Finite element modelling of flat punch indentation

2.1. The strain-gradient plasticity model

A range of conceptual and numerical strain-gradient plasticity models have been proposed and experimentally investigated (De Guzman et al., 1993; Fleck and Hutchinson, 1997; Gao et al., 1999; Gurtin, 2000, 2002; Huang et al., 2006; Kiener et al., 2009; Ma and Clarke, 1994; Nix and Gao, 1998; Oliver and Pharr, 1992; Pharr et al., 2010; Swadener et al., 2002). The reader is directed towards Evans and Hutchinson (2009) for a critical assessment of these models. In this paper the spatially and temporally varying yield stress of the strain-gradient plasticity model (1) proposed by Nix and Gao (1998) is implemented in rate form using the Garofalo creep model (Garofalo, 1965)

$$\dot{\gamma}_p = A \sinh\left(\frac{\tau_e - \tau_Y}{\tau_{ref}}\right) \tag{6}$$

where $\dot{\gamma}_p$ is the plastic shear strain rate, A and τ_{ref} are constant creep parameters, $\tau_e = \frac{1}{\sqrt{3}}\sigma_e$ is the effective shear stress, σ_e is the effective (von Mises) stress and we take $\tau_e - \tau_Y = 0$ if $\tau_e < \tau_Y$. As the indentation is not intended to be rate-dependent, the final solution should not be too sensitive to the form of the rate model selected, i.e. yielding and subsequent plastic relaxation occur rapidly if $\tau_e > \tau_Y$. Eq. (6) has a physical basis (Gao et al., 1999) but the creep parameters are chosen such that the quasi-static solution $\tau_e = \tau_Y$ is achieved within a characteristic time that is very much less than the time taken to complete the indentation test. We take a Young's modulus of $E = 70$GPa, Poisson ratio $\nu = 0.3$, a SSD density of $\rho_S = 10^{12}\text{m}^{-2}$, $A = 1\,\text{s}^{-1}$ and $\tau_{ref} = 50$MPa. The ISE manifests noticeably once the GND density is of a similar order of magnitude to ρ_S. This choice therefore influences the punch size at which the ISE is observed in the FE model. The initial normal yield stress (before forest hardening) is taken as $\sigma_{y0} = 100$MPa. The local GND density is calculated using the Nye equation

$$\rho_G = \frac{1}{\text{b}}|curl[F_p]| \tag{7}$$

where $[F_p]$ is the plastic part of the deformation gradient tensor. The detailed expressions derived from (7) for the plain strain and axisymmetric cases are given in Appendix A. The model was implemented in COMSOL Multiphysics v5.3 using an unstructured triangular mesh of quadratic isoparametric elements. The plastic strain derivatives are not directly available in COMSOL and were calculated by integrating the plastic strain rates over time using domain ordinary differential equations and evaluating the spatial gradients of this additional field. Interfacial friction between the indenter and the substrate material is neglected.

2.2. Validation of the finite element ISE model for conical and spherical indenters

The predictions of the Nix and Gao (1998) model for conical and Swadener et al. (2002) model for spherical indenters are used to test the proposed finite element model. The models of (3) and (4) are greatly simplified, so exact comparison is not anticipated, but the correct scaling of the ISE is expected to be reproduced. The results of axisymmetric simulations for rigid spherical indenters with a range of different radii are shown in Fig. 1. The average GND density is shown in Fig. 1a along with a fit to the theoretical prediction. In the simulations, the GND density is found in practice to be highly inhomogeneous. The total GND length is found by integrating the GND density defined by (7) over the entire volume of the substrate. The average GND density, as defined by the Nix–Gao models, is then the total length divided by the volume of a hemisphere of radius c. The prediction that the average GND density is constant and does not change with strain is clearly evident. The best fit is given by $\rho_G = \frac{0.025}{bR}$, which is 2.5% of the value estimated by the model of Eq. (4). This is not surprising given the very simple assumptions made about the geometry. This now suggests that $R^* = \frac{0.025}{b\rho_S} = 100\ \mu m$. Fig. 1b demonstrates that for spherical indenters the hardness also does not change with the indentation depth (represented here by the strain c/R) as predicted. The best fit for (4) is shown, with $H_0 = 0.72$ GPa and $R^* = 90$ µm, compared to the estimated values of $H_0 = 0.3$ GPa and $R^* = 100$ µm from the simple theory.

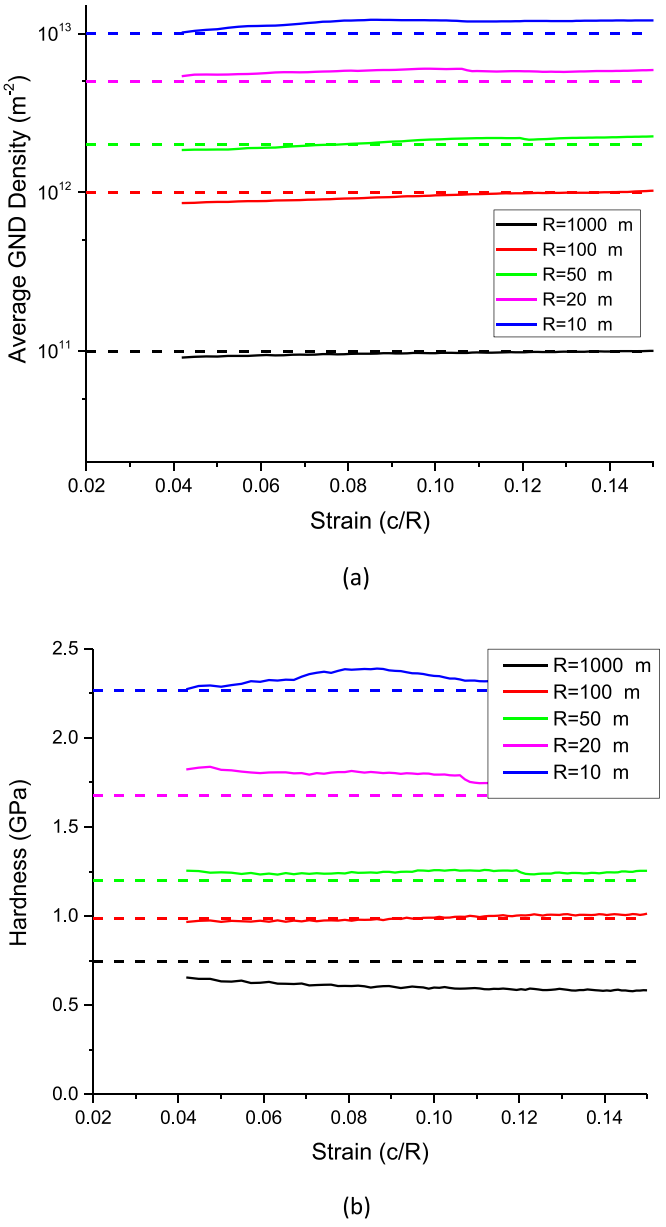

Fig. 1. Results of strain gradient finite element simulations for spherical indenters of different radii $\boldsymbol{R}$ compared with the predictions of Swadener et al. (4) for (a) average GND density against strain ($\boldsymbol{c/R}$), and (b) hardness against strain. Values are only shown after significant indentation has occurred for strains above 4%.

Similarly, results for simulations with conical indenters are shown in Fig. 2. A small tip radius was introduced to the cone

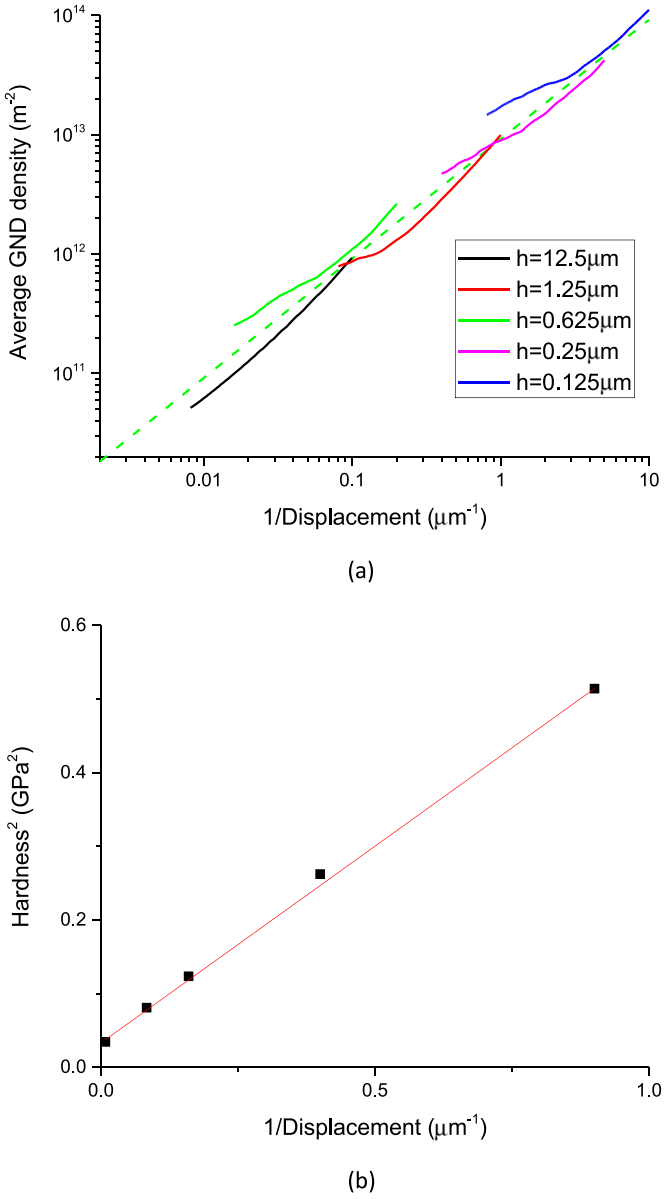

Fig. 2. Results of strain gradient finite element simulations for a conical indenter at different indentation depths δ compared with the predictions of Nix–Gao (3) for (a) average GND density against reciprocal of indentation depth, and (b) hardness squared against the reciprocal of indentation depth $1/\delta$.

point for numerical stability during the initial part of the loading stage, although it was too small to have a significant effect on the results, with its height equivalent to 3% of the maximum displacement. The cone angle (with respect to the horizontal) was 5°. Fig. 2a shows the average GND density against the reciprocal of the indentation depth $1/h$ on a log-log plot compared with the predictions of the Nix–Gao model, $\rho_G = \frac{3\tan^2\theta}{2bh}$. Again, the local GND density is highly inhomogeneous in the simulation, but the average scales well with simple estimates, although the (dashed) line of best fit is 20% of the predicted value. The scaling of the hardness squared is also predicted by Eq. (3) to be a linear function of the reciprocal indentation depth, and the consistency between the simulation results and the Nix–Gao model is clear in Fig. 2b. The best fit is obtained for $H_0 = 0.18$ GPa compared to the estimated value of $H_0 = 0.3$ GPa. The reduced average GND density suggests that we should take 20% of the predicted value of $h^* = 46$ μm. This

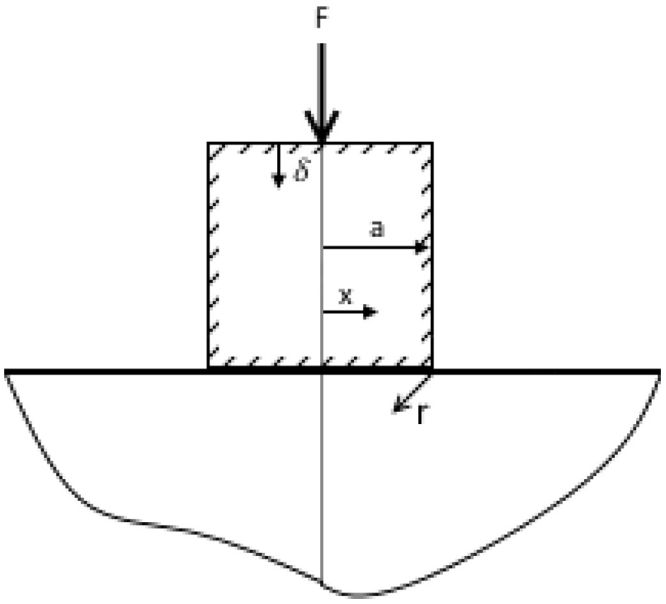

Fig. 3. Geometry of the plain strain flat punch indentation model.

reduced value of $h^* = 9.2$ μm agrees favourably with the best fit value of $h^* = 16$ μm within the approximations taken.

Overall the general scaling of (3) and (4) represent the material response well, and the fact that the actual geometric factors are different from those estimated in the derivation of (3) should not be too surprising within such a difference between the simplicity of the deformation field proposed within the Nix–Gao analytical model and the highly inhomogeneous and localised deformation field seen in the numerical model. The important observation is that both models produce the same experimentally observable trends, but that experimentally determined values require a correction factor to be related back to the Nix–Gao parameters directly. These simulations have demonstrated the proposed finite element models capacity to reproduce the ISE predicted by the Nix–Gao models with reasonable accuracy for both conical and spherical indenters. The approach is now extended to consider a flat punch indenter in the following section.

2.3. Simulation results for a flat punch indenter

The geometry for flat punch indentation is simple and is shown in Fig. 3. A rigid flat indenter of half-width a is displaced downwards a distance δ into the substrate under 2D plain strain conditions. The force is recorded as the indenter is pressed into the substrate and as it is retracted. The mesh is refined around the edges of the punch where the highest stresses occur.

Loading and unloading curves for normalised mean indentation pressure against normalised indentation depth are shown in Fig. 4. The pressure P is normalised by the macroscopic yield pressure P_{y0} and the indentation depth δ is normalised by the width of the indenter $2a$. All the curves demonstrate an approximately elastic response at the commencement of loading, although in practice small amounts of plasticity initiate at the sharp edges of the punch almost immediately. For the largest punch, of total width $2a = 10$ mm, the pressure levels off once the macroscopic yield pressure P_{y0} is reached, demonstrating no hardening due to strain gradients. The elastic unloading curve is parallel to the elastic part of the loading curve as expected. Overall the curves look very similar to experimental curves (Riccardi and Montanari, 2004). Smaller punches demonstrate increasingly large elastic contributions to the

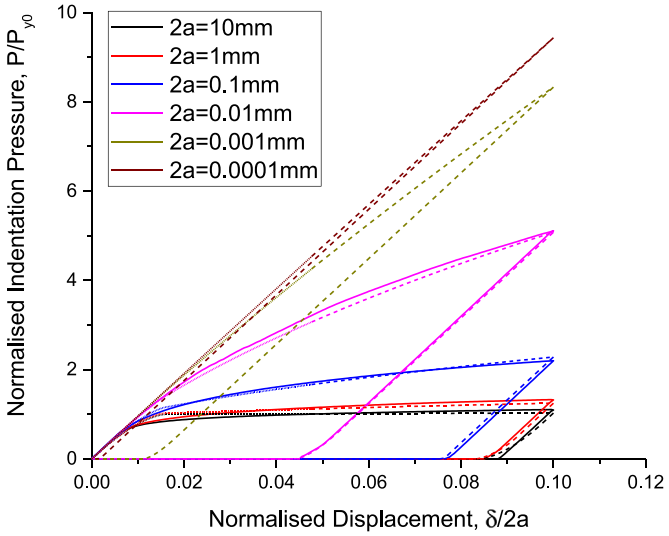

Fig. 4. Simulations results for normalised mean indentation pressure P/P_{y0} against normalised indentation depth $\delta/2a$ calculated for flat punches of different widths $2a$. The solid lines are the finite element simulation results, and the dashed lines are the predictions of the analytical model for loading (22) and unloading (27).

initial loading stage, with increasingly localised plastic hardening around the edges as the indentation width decreases.

Fig. 5 shows the change in morphology of the plastic zone with indenter size. The plastic region starts to form at the edge of the punch in each case. In the large punch case, Fig. 5a, the GND density remains low, resulting in little plastic hardening at the edges and growth of the edge plastic zones via load transfer until they meet in the middle and form a roughly hemispherical plastic zone under the indenter. This is similar to the expanding cavity model of Johnson (1987) adopted for modelling flat punch indentation. Here the plastic zone is relatively small and the plastic strains are high. The small punch case, shown in Fig. 5b, is quite different. The plastic zones at the edges experience highly localised strain gradient hardening. This results in a relatively larger plastic zone within which the plastic strains are much lower. A pre-dominantly elastic region of hydrostatic pressure forms under the indenter in this case. Therefore, unlike spherical and self-similar indentation, there is expected to be a clear visual difference between the shape of the plastic zone at different length scales. If explored experimentally, these cases have the potential to provide insight into the contrasting nature of plasticity at different scales which is not so readily available in other nanoindentation test methods. Similar simulations performed using the Fleck-Hutchinson strain gradient plasticity model show a similar but not identical trend to the one shown in Fig. 4, albeit across a smaller range of indenter widths (Evans and Hutchinson, 2009).

The ISE determined from the flat punch finite element simulations for a fixed indentation depth-to-width ratio of $\frac{\delta}{2a} = \frac{1}{10}$ is presented in Fig. 6. The pressure squared, P^2, is plotted as a function of the reciprocal of the punch half-width, $\frac{1}{a}$, in the spirit of the Nix–Gao ISE models, such that the empirical model for the ISE in flat punches proposed by Chen et al. (2010), Eq. (5), predicts that the data will lie on a straight line. Extrapolating the near-macroscopic punch data gives the linear fit for (5) shown, whereas the best fit to the finite element simulation results is given by the analytical model (22) developed in the next section. Given the differences between the flat punch case and the spherical and self-similar indentation cases, it is not surprising that (5) does not completely capture the ISE for flat punches, although it can be reasonably effective over a small range of sizes. To gain further insight into the mechanisms behind the ISE in flat punch indentation, a full elasto-plastic analytical model is developed in the next section and validated against the finite element results reported here, as seen in Figs. 4 and 6. A closed form for this indentation pressure as a non-linear function of both the punch width and

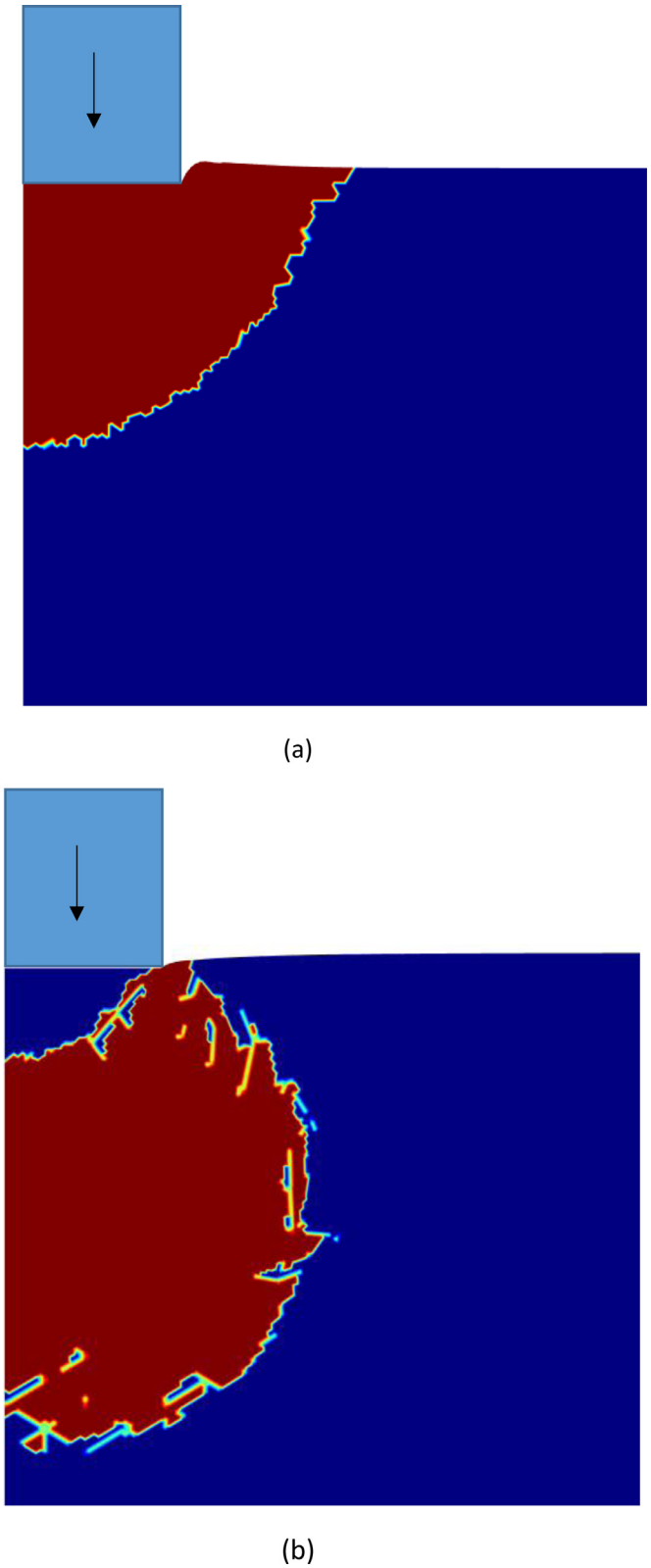

Fig. 5. Strain gradient finite element half-symmetry simulations of the (red) plastic zone, defined to be where the effective plastic strain is greater than 1%, for flat punch indenters of width (a) $2\boldsymbol{a} = 10\mathbf{mm}$, and (b) $2\boldsymbol{a} = 0.01\mathbf{mm}$, after an indentation of depth $\boldsymbol{\delta} = 2\boldsymbol{a}/10$. The jagged boundaries are due to small numerical perturbations.

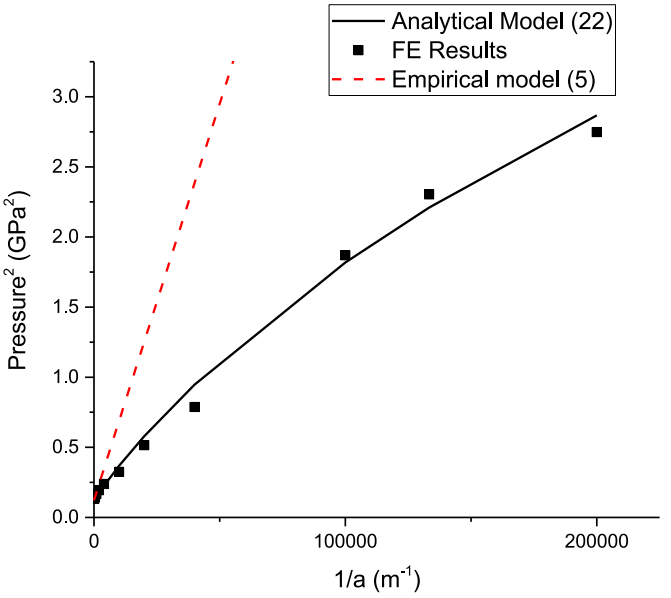

Fig. 6. Strain gradient finite element flat punch simulation results for the square of the indentation pressure $\boldsymbol{P}^2$ against the reciprocal of the indenter half-width, $\frac{1}{a}$. The empirical prediction (5) is shown as a red dashed line, with the results of the proposed analytical model (22) in black.

the indentation depth is derived. By its nature, it is more complex than the simple rules provided by (3) and (4), but it is still readily evaluated numerically.

3. An analytical model for the flat punch ISE

3.1. Derivation of a Nix–Gao type model for flat punch indentation

The plane strain elasticity solution for the (elastic) pressure under a rigid flat frictionless indenter of half-width a is given by (Johnson, 1987)

$$p_e(x) = \frac{F_e}{\pi\sqrt{a^2 - x^2}} \tag{8}$$

where x is the lateral distance from the centre of the punch and

$$F_e = \int_{-a}^{a} p(x)dx = k_e\delta_e \tag{9}$$

is the applied downward force (per unit length). This is expected to be proportional to the elastic displacement δ_e through a stiffness constant k_e which will depend on the Young's modulus and Poisson's ratio of the substrate. A representation of this elastic pressure distribution (8) can be seen in Fig. 7a. Importantly it can be seen that there is an infinite pressure at the edges of the punch. This will necessarily result in the early onset of plasticity at the edges.

Slip-line theory (Calladine, 1985) provides an exact solution for the pressure required to cause generalised yielding of a perfectly plastic material under a flat punch ignoring the contribution from elasticity

$$p_{Y0} = \sigma_{Y0}\left(1 + \frac{\pi}{2}\right) \tag{10}$$

where σ_{Y0} is the perfectly plastic yield stress. A possible deformation mechanism for the slip line field near an edge is shown in the substrate in Fig. 7b, whereby slip occurs below the indenter and propagates along the slip lines towards the free surface as shown. Here we make a number of assumptions to extend this model to generate an approximate model for the response of the full elasto-plastic case, where only partial plastic deformation has occurred under the indenter, as shown in Fig. 7b. Plasticity is assumed to initially occur under the corners of the indenter, generating a localised plastic zone. As the displacement of the punch increases, the plastic zone is expected to increase until the two edge plastic zones meet in the middle, at which point full plastic deformation of the substrate is said to have occurred. The complex load transfer process is greatly simplified such that the maximum pressure is capped at the yield pressure, as shown in Fig. 7b. This yield pressure will monotonically increase due to strain gradient hardening leading to the ISE.

To progress with this model we write the total displacement of the substrate at the interface with the rigid indenter as the sum of elastic (e) and plastic (p) components

$$\delta = \delta_e(x) + \delta_p(x) \tag{11}$$

where δ is the uniform prescribed indentation displacement, but its elastic and plastic components are spatially varying along the interface. The aim of the model is now to determine the elasto-plastic pressure distribution under the rigid punch, $p(x)$, to determine the applied force require to achieve the displacement. From (8) we define the plastic displacement component as

$$\delta_p(x) = \delta - \frac{\pi}{k_e}\sqrt{a^2 - x^2}\,p(x) \tag{12}$$

This satisfies the requirement that there is no plastic strain ($\delta = \delta_e$) when the pressure distribution is fully elastic ($p(x) = p_e(x)$). It is expect to be closely related to the shape of the plastic indent but not exactly the same. This is because the stress redistribution due to yielding is not precisely accounted for.

As described above, a simple approximation for the elasto-plastic pressure distribution is assumed, such that it varies from both corners as

$$p(r) = \begin{cases} p_e(r) & if\ r_p < r < a \\ p_Y(r) & if\ 0 < r < r_p \end{cases} \tag{13}$$

where $r = a - x$ is the distance from an edge, and r_p is the radius of the plastic zone at the punch edges, as shown in Fig. 7b. The latter is determined from the condition that the elastic pressure is equal to the initial yield pressure (before hardening), i.e. $p_e(r_p) = p_{Y0}$. The resulting plastic zone radius can therefore be expressed as a function of the indentation depth as

$$r_p(\delta) = \begin{cases} a\left(1 - \sqrt{1 - \left(\frac{\delta}{\delta_0}\right)^2}\right) & \text{if } 0 < \delta < \delta_0 \\ a & \text{otherwise} \end{cases} \tag{14}$$

where $\delta_0 = \frac{\pi a p_{Y0}}{k_e}$ is a characteristic length scale, which depends on the test length scale a and a ratio of the elasto-plastic properties of the substrate. We now introduce strain gradient plastic hardening through the Nix–Gao formulation previously used, (2), with Eq. (10), to write the plastic yield pressure under the indenter as

$$p_Y = p_{Y0}\sqrt{1 + \frac{\rho_G}{\rho_S}} \tag{15}$$

The GND density (7) is proportional to the plastic strain gradient and the reciprocal of the materials Burger's vector b. The strain field under the indenter is not known, but it is reasonable to assume that it will scale with the plastic component of displacement δ_p and the size of the punch a. The strain is higher nearer the edges of the punch and hence, to make an analytical solution feasible, the following empirical form for the GND density is proposed

$$\rho_G(r) = \frac{\alpha\delta_p(r)}{ba^2}\left(\frac{a}{r}\right)^n \tag{16}$$

where n is an exponent and α is a dimensionless geometric parameter. It is expected that $0 < n < 2$ as n must be greater than

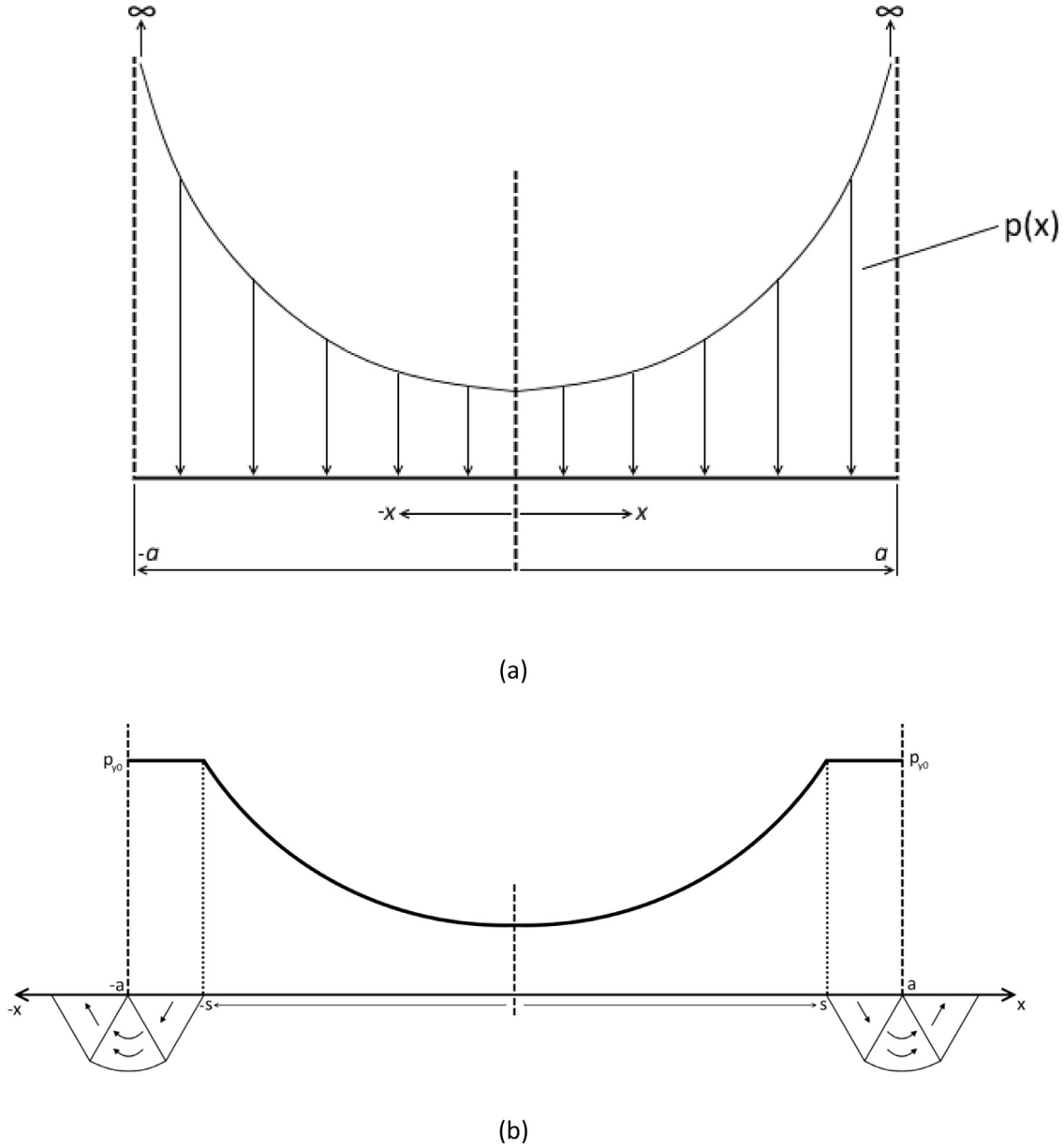

Fig. 7. (a) Purely elastic solution (8) for the pressure distribution under a flat punch for frictionless conditions, and (b) proposed elasto-plastic pressure distribution for perfectly plastic yield pressure of $\boldsymbol{p_{y0}}$, showing possible slip deformation mechanism in the substrate at the punch edges.

zero for a peak density at the punch edges, and the strength of the singularity becomes too large for values of $n \geq 2$, leading to a non-finite mean indentation pressure, as defined by (21). These will be calibrated to best fit the simulation results. Eqs. (12), (15) and (16) can now be combined to generate the following quadratic for the plastic yield pressure as a function of position in the yielded region

$$\beta \bar{r}^n \bar{p}_Y^2 + \sqrt{\bar{r}(2-\bar{r})}\,\bar{p}_Y - \left(\beta \bar{r}^n + \bar{\delta}\right) = 0 \tag{17}$$

where the following dimensionless quantities have been introduced

$$\bar{p}_Y = \frac{p_Y}{p_{Y0}} \quad \bar{\delta} = \frac{\delta}{\delta_0} \quad \bar{r} = \frac{r}{a} \tag{18}$$

in addition to a characteristic dimensionless parameter

$$\beta = \frac{b k_e \rho_s}{\alpha \pi\, p_{Y0}} a \tag{19}$$

which scales with the punch width a. The quadratic (17), combined with (8) and (13), yields the total pressure distribution under the punch

$$\bar{p}(\bar{r}) = \begin{cases} \dfrac{\bar{\delta}}{\sqrt{\bar{r}(2-\bar{r})}} & \text{if } \bar{r}_p < \bar{r} < 1 \\ \dfrac{\sqrt{\bar{r}(2-\bar{r})}}{2\beta \bar{r}^n}\left[\sqrt{1 + \dfrac{4\beta \bar{r}^n \left(\beta \bar{r}^n + \bar{\delta}\right)}{\bar{r}(2-\bar{r})}} - 1\right] & \text{if } 0 < \bar{r} < \bar{r}_p \end{cases} \tag{20}$$

The total normalised average indentation pressure is then determined using (9)

$$\bar{P} = \int_0^1 \bar{p}(\bar{r}) d\bar{r} = \int_{\bar{r}_p}^1 \bar{p}_e(\bar{r}) d\bar{r} + \int_0^{\bar{r}_p} \bar{p}_Y(\bar{r}) d\bar{r} \tag{21}$$

where $\bar{P} = \frac{P}{p_{y0}} = \frac{F}{2a p_{Y0}}$.

Solving (21) numerically, it is found that the level of elastic recovery increases with n, and that the best correspondence with the simulation results is very clearly obtained when $n = 1$. Hence this value is selected for further inspection. An additional benefit is

that the plastic integral (21) can be solved analytically for the case of $n=1$. The final model for the normalised indentation pressure during loading (L) as a function of the normalised displacement $\bar{\delta}$ is given by

$$\bar{P}_L = \bar{\delta}\sin^{-1}(1-\bar{r}_p) + \frac{1}{2\beta}\left[\sqrt{2+4\beta\bar{\delta}}\; g\left(\bar{r}_p, \frac{4\beta^2-1}{2+4\beta\bar{\delta}}\right) - \sqrt{2}\; g\left(\bar{r}_p, -\frac{1}{2}\right)\right] \tag{22}$$

where $\bar{r}_p = \begin{cases} 1-\sqrt{1-\bar{\delta}^2} & \text{if } 0<\bar{\delta}<1 \\ 1 & \text{if } \bar{\delta}\geq 1 \end{cases}$ and

$$g(x,y) = \sqrt{x(1+xy)} + \begin{cases} \frac{1}{\sqrt{y}}\arcsin h\sqrt{xy} & \text{if } y>0 \\ \frac{1}{\sqrt{-y}}\arcsin\sqrt{-xy} & \text{if } y<0 \end{cases} \tag{23}$$

The unloading (UL) phase is modelled by assuming that the elastic solution, $\bar{p}_e(\bar{r})$, given by Eq. (8), is subtracted from the final elasto-plastic pressure distribution, $\bar{p}_m(\bar{r})$, obtained at the end of the loading phase. If the peak indentation depth is $\bar{\delta}_m$ then the peak pressure state is

$$\bar{p}_m(\bar{r}) = \begin{cases} \frac{\bar{\delta}_m}{\sqrt{\bar{r}(2-\bar{r})}} & \text{if } \bar{r}_{pm}<\bar{r}<1 \\ \frac{\sqrt{\bar{r}(2-\bar{r})}}{2\beta\bar{r}}\left[\sqrt{1+\frac{4\beta(\beta\bar{r}+\bar{\delta}_m)}{(2-\bar{r})}}-1\right] & \text{if } 0<\bar{r}<\bar{r}_{pm} \end{cases} \tag{24}$$

where $\bar{r}_{pm} = \begin{cases} 1-\sqrt{1-\bar{\delta}_m^2} & \text{if } 0<\bar{\delta}_m<1 \\ 1 & \text{if } \bar{\delta}_m\geq 1 \end{cases}$. Without adhesion between the punch and the substrate, the total pressure, $\bar{p}_{UL} = \bar{p}_m - \bar{p}_e$, must be positive if the surfaces are in contact, and zero if they separate. Hence, at an unloading displacement of $0\leq\bar{\delta}\leq\bar{\delta}_m$ the pressure distribution is approximated as

$$\bar{p}_{UL}(\bar{r}) = \begin{cases} \frac{\bar{\delta}}{\sqrt{\bar{r}(2-\bar{r})}} & \text{if } \bar{r}_{pm}\leq\bar{r}\leq 1 \\ \frac{\sqrt{\bar{r}(2-\bar{r})}}{2\beta\bar{r}}\left[\sqrt{1+\frac{4\beta(\beta\bar{r}+\bar{\delta}_m)}{(2-\bar{r})}}-1\right] - \frac{(\bar{\delta}_m-\bar{\delta})}{\sqrt{\bar{r}(2-\bar{r})}} & \text{if } 0\leq\bar{r}\leq\bar{r}_{pm} \end{cases} \tag{25}$$

The unloading of the plastic zone needs to be considered with some care, to avoid the pressure defined in the plastic region $0\leq\bar{r}\leq\bar{r}_{pm}$ becoming negative. The critical radius within the plastic zone at which contact is lost is given by $\bar{r}_0 = (1-\frac{\bar{\delta}}{2\beta}) \pm (1+\frac{\bar{\delta}}{2\beta})\sqrt{1-\frac{(\bar{\delta}_m-\bar{\delta})^2}{(1+\frac{\bar{\delta}}{2\beta})^2}}$, defined by the condition that $\bar{p}_{UL}=0$. There are two possible values of $\bar{r}_0$. The value of $\bar{r}_0$ that is real and between 0 and 1 is taken. If neither value satisfies this condition, $\bar{r}_0$ is taken to be zero. Inspection shows that there are two different scenarios that can occur. Case I is where separation of the surfaces starts at the edges. In this case, contact is lost in the region $0\leq\bar{r}\leq\bar{r}_0$ with $\bar{r}_0$ increasing from 0 to $\bar{r}_{pm}$ as the unloading progresses. Case II relates to the situation where the punch first loses contact with the surface from the middle. In this case, contact is lost in the region $\bar{r}_0\leq\bar{r}\leq\bar{r}_{pm}$, with $\bar{r}_0$ decreasing from $\bar{r}_{pm}$ to 0 as the unloading progresses. The two situations are differentiated using the plastic zone pressure, $\bar{p}_{UL}(1)$, calculated at the centre of the punch where $\bar{r}=1$. Observing that the pressure changes monotonically with the distance from the edge, case I occurs if $\bar{p}_{UL}(1)>0$ during separation, and case II occurs if this is not true. We introduce the following variable to choose between these cases, such that

$$\gamma = \begin{cases} 0 & \text{if } \bar{\delta}<\bar{\delta}_c \\ 1 & \text{if } \bar{\delta}\geq\bar{\delta}_c \end{cases} \tag{26}$$

where $\bar{\delta}_c = \bar{\delta}_m + \frac{1}{2\beta}(1-\sqrt{1+4\beta(\beta+\bar{\delta}_m)})$.

The force during unloading is now the integral of the net pressure under the indenter such that

$$\bar{P}_{UL} = \bar{\delta}\arcsin(1-\bar{r}_{pm}) - (\bar{\delta}_m-\bar{\delta})\Big[(1-\gamma)\frac{\pi}{2} + (2\gamma-1)(\arcsin(1-\bar{r}_0)+\gamma\arcsin(1-\bar{r}_{pm}))\Big] + \frac{\sqrt{2+4\beta\bar{\delta}_m}}{2\beta} \times\left[\gamma g\left(\bar{r}_{pm}, \frac{4\beta^2-1}{2+4\beta\bar{\delta}_m}\right) + (1-2\gamma)g\left(\bar{r}_0, \frac{4\beta^2-1}{2+4\beta\bar{\delta}_m}\right)\right] - \frac{1}{\sqrt{2}\beta}\left[\gamma g\left(\bar{r}_{pm}, -\frac{1}{2}\right) + (1-2\gamma)g\left(\bar{r}_0, -\frac{1}{2}\right)\right] \tag{27}$$

3.2. Comparison between numerical and analytical models

The analytical models for the loading (22) and unloading (27) curves are readily calculated. The size effect is determined by the parameter β. We have $\rho_S = 10^{12}\text{m}^{-2}$ and $b = 0.25\times10^{-9}\text{m}$. For a Young's modulus of $E=70$ GPa and Poisson ratio $\nu=0.3$ we find $k_e = 32$ GPa. For an initial yield stress of $\sigma_{y0}=100$MPa we find the simulated perfectly plastic yield pressure is $p_{y0}=333$ MPa, a little higher than the 257 MPa predicted by the simple slip line theory of (10). A best fit is obtained when $n=1$ and when the dimensionless GND scaling parameter is $\alpha=0.087$ meaning that (17) can be expressed as $\beta = 88,000\,\text{m}^{-1}\times a$. A comparison of the results obtained from the finite element simulations is presented in Figs. 4 and 6 for several different indenter widths. Given the numerous simplifications adopted to develop the analytical model, the close correspondence between the two solutions is exceptionally good. The numerical simulation has difficulty converging for the very demanding cases of $2a=0.001$mm and smaller, but the analytical solution predicts that plastic hardening at the corners is so intensive at these very small scales, and that the response tends towards being almost fully elastic.

Fig. 8 shows the indentation pressure at an indentation depth of $\delta=2a/10$ predicted by (22). The horizontal axis is $\log_{10}(2a)$ as the flat punch ISE is illustrated across punch widths of six orders of magnitude, from 10 nm up to 10 mm. The FE results are also shown

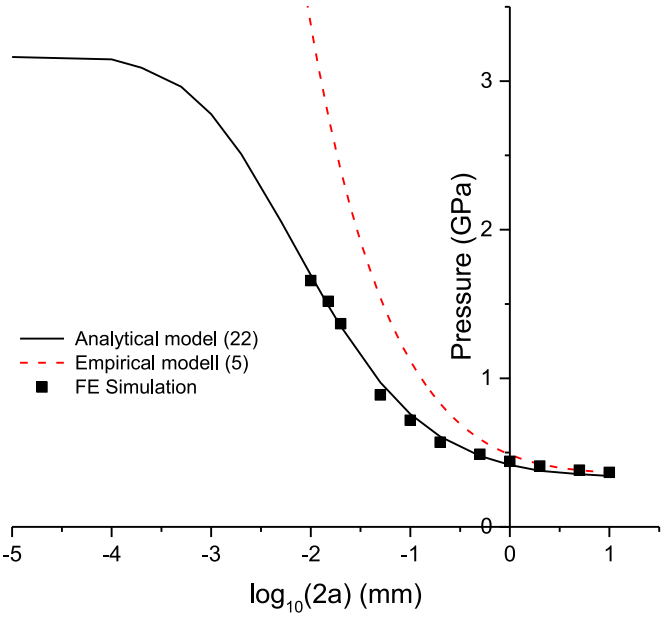

Fig. 8. Indentation pressure vs log of punch width $2a$ comparing the model with the results of strain gradient finite element simulations, and the empirical model of Eq. (5).

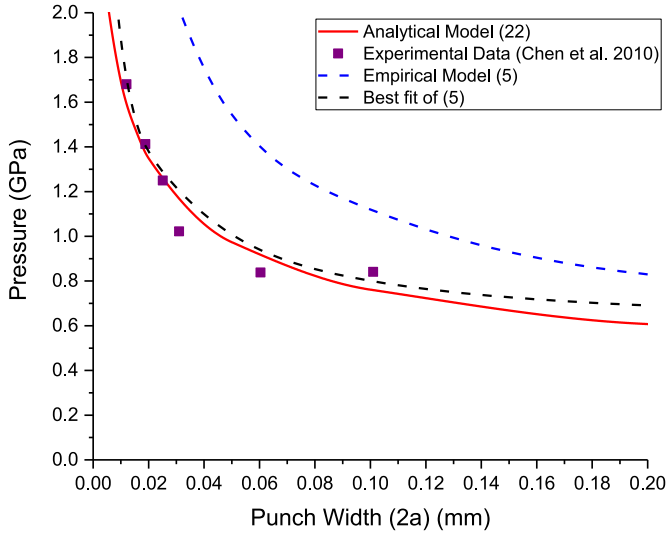

Fig. 9. Comparison of different models against experimental data (Chen et al., 2010): the analytical model (22), best fit of (5) to the experimental data, a fit of (5) from the predicted near-macroscopic response. .

for punch widths ranging from 0.001 mm to 10 mm. The correspondence is extremely good. It was not possible to perform the FEM simulations for indenter widths of below $2a = 0.001$mm due to convergence problems with the highly intensive strain-gradient hardening at the sharp edges. The indentation pressure plateaus at the elastic limit, $P_e = \frac{F_e}{2a} = \frac{k_e \delta_e}{2a} = \frac{k_e}{10} = 3.2$ GN/m, once the flat punch gets below a certain size, as plasticity is then so localised at the edges that the substrates response to the indenter is almost fully elastic, providing a natural upper bound to the indentation pressure. This response is because the GND density at the edges becomes extremely large. Whether this is a physically realistic assumption of the model is investigated in Section 4.

3.3. Comparison with experimental results

The experimenal results of Chen et al. (2010) for rectangular strip punch indentation of aluminium single crystals demonstrate the existence of the ISE for flat punches. They determine a characteristic indentation pressure and plot it against the punch width. The data is reproduced in Fig. 9 and compared with the predictions of the various models proposed here. The two unknowns in Eq. (5) are optimised to best fit the data, and it is shown that it models the data quite well across the decade of punch sizes considered, from 0.55μm to 5μm. The parameters of the analytical model (22) are also chosen to fit the experimental data, and the fit is very similar to (5) over the relatively small size range considered. However, if the near-macroscopic curve from the analytical model (22) is used to determine the parameters of (5), then the fit is not particularly good. As we have seen in Fig. 8, Eq. (5) can be used to provide a good linear fit the data over a narrow size range but it is not valid across a wide range of sizes.

4. Further analysis of the flat punch ISE using the analytical model

4.1. Effect of rounded edges

In practice, a real flat punch indenter will not have perfectly sharp edges. The importance of the finite curvature of the edges is likely to become more significant as the size of the punch diminishes. To investigate this, finite element simulations were conducted with a fixed edge radius of 0.01μm. It was found that there was no significant difference between the force-displacement curves with sharp and rounded edges, except that the round edged simulations helped improve the numerical convergence of the model and as such could be conducted for very small punches with very substantial strain gradient hardening. Encouragingly, these simulations were found to agree very closely with the predictions of the analytical model seen in Fig. 4.

4.2. Removing the ρ_S dependence from the hardness model

One observation about the forest hardening approach used in the Nix–Gao approach (15) is that it relies on the existence of an often very significant initial SSD population in the test sample. However, this is often an assumption that cannot be readily justified. Recent work by Campbell and Gill (2019) has demonstrated that (15) can be equally well replaced by

$$p_Y = p_{Y0} + \eta\sqrt{\rho_G} \tag{28}$$

without a visibly significant change in the quality of the fit to the data, where $\eta = (1 + \frac{\pi}{2})\sqrt{3}\beta_F G b$. This model assumes that the macroscopic strength of the material is not due to SSD forest hardening, but due to other mechanisms, e.g. intrinsic strength, precipitation hardening, solid solution strengthening etc. In general it is found that, when fitting the parameters to known data, the underlying physical parameters are in the expected range, which was not found to be the case for (3) and (4). Replacing (15) by (28) in the model changes (17) to the following

$$\beta' \bar{r}^n \bar{p}_Y^2 + \left[\sqrt{\bar{r}(2-\bar{r})} - 2\beta'\right]\bar{p}_Y + \left(\beta' \bar{r}^n - \bar{\delta}\right) = 0 \tag{29}$$

where

$$\beta' = \frac{b k_e p_{Y0}}{\alpha \pi \eta^2} a \tag{30}$$

now no longer depends on the initial SSD density ρ_S. To avoid further lengthy analytical manipulations, the pressure is determined from the quadratic (29) for a given displacement $\bar{\delta}$ and position $\bar{r}$ and integrated according to (21) numerically. It is found that, as expected, the results for the revised constitutive model (28) are not significantly different to those found previously if we take $\eta = p_{y0}/\sqrt{\rho_s}$. The real reason for the change in the constitutive law is preparation for the next section for which physically realistic parameters are necessary.

4.3. Limiting the maximum value of ρ_G

It was noted in Section 3.2 that the very high indentation pressures achieved at very low punch widths were a result of the GND density reaching extremely high values at the edges. Theoretically there is an upper limit to the dislocation density, with the purely geometrical limit of $\frac{1}{b^2} = 16x10^{18}\text{m}^{-2}$ being the extreme upper value. The latter is not physically possible of course but it gives insight into the expected, acceptable range of this parameter. A typically observed value (Pharr et al., 2010) is a maximum GND density of $\rho_m \approx 10^{16} m^{-2}$. Following Campbell and Gill (2019) the inverse sum rule is used to determine the actual GND density such that, using (16)

$$\frac{1}{\rho_G} = \frac{b a^2 \bar{r}^n}{\alpha \delta_p(r)} + \frac{1}{\rho_m} \tag{31}$$

This can then be combined with (12) and (28) to derive the pressure distribution, and hence the total contact pressure from (21). The parameter $\chi = (\frac{p_{y0}}{\Delta p_{ym}})^2$ is employed to characterise the cap on the maximum dislocation density, where $\Delta p_{ym} = \eta\sqrt{\rho_m}$ is the maximum increase in the yield pressure due to strain gradient hardening and $0 \le \chi \le \infty$. The case of $\chi = 0$ corresponds to

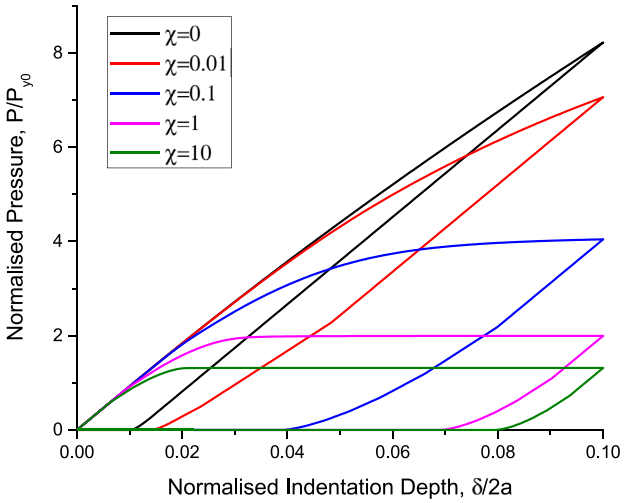

(a)

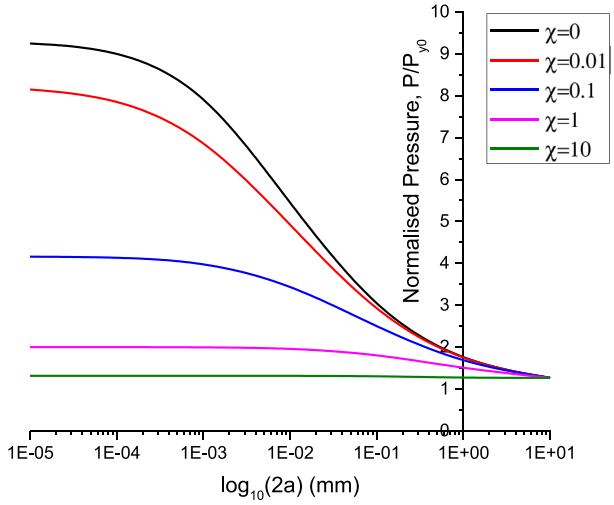

(b)

Fig. 10. Effect of capping the maximum allowable GND density. (a) Normalised pressure vs indentation depth loading/unloading curves for punch width $2a = 0.001$ mm, and (b) peak normalised pressure for a final indentation depth of $\frac{\delta}{2a} = \frac{1}{10}$. Both are shown as a function of χ. The maximum normalised yield pressure is $1 + \chi^{-0.5}$, so $\chi = 0$ has unbounded yield stress, with the maximum allowable value decreasing as χ gets larger.

no limit on strain gradient hardening, and hence should reproduce the results of Figs. 4 and 6 for a given punch width. The case of $\chi = \infty$ corresponds to no hardening such that the perfectly plastic results for macroscopic indentation ($a \to \infty$) are reproduced. Fig. 10a shows the effect of capping the maximum dislocation density on the normalised pressure vs indentation depth curves for a punch of width $2a = 1$ μm. Fig. 10b shows how the peak hardening response is affected as a function of the punch width. As expected, the peak indentation pressure is reduced as χ increases. In practice, an order of magnitude increase in the yield stress due to strain gradient plasticity is not unreasonable, suggesting that values around $\chi = 0.01$ are to be physically expected. Fig. 10b therefore suggests that the observed flat punch ISE with a limit on the maximum GND density is only expected to be 10–20% lower than that anticipated without a limit.

5. Conclusion

An analytical expression for the indentation size effect (ISE) in plane strain flat punch indentation has been proposed. The model uses the Nix–Gao strain gradient plasticity model to accurately reproduce the force-displacement loading and unloading response of a flat punch indentations of different widths predicted by finite element simulation. The flat punch ISE has been demonstrated to occur in aluminium (Chen et al., 2010) and the proposed model can reproduce these observations well. The flat punch ISE is of interest as it differs from the Nix–Gao models for self-similar and spherical indenters in a number of ways: (1) the contact area does not change; (2) the contact pressure depends on two length scales not just one (the punch width and the indentation depth); (3) the profile of the punch is not differentially continuous, resulting in singular plastic strain gradients at the sharp edges, such that (4) the shape and connectivity of the plastic zones change with indentation depth and punch width, resulting in (5) important changes in the proportion of the deformation accommodated by elasticity and plasticity, meaning that a fully elastoplastic model is required. The model is extended to incorporate the consequence of imposing natural limitations on the maximum dislocation density at the edges. It is suggested that observable changes in the plastic zone morphology with the ISE make this an experimentally interesting area for future investigation and validation of size effects in plasticity.

Acknowledgements

This work was performed as part of a EURAMET joint research project (StrengthABLE) with funding from the European Community's Seventh Framework Programme, ERA-NET Plus, under Grant agreement no. 217257.

Appendix

Determination of **curl**[**F**] *in rectangular and cylindrical coordinates*

Write the deformation tensor as the sum of the various components

$$[F] = \sum_i \sum_j F_{ij} \underline{e}_i \otimes \underline{e}_j \tag{A1}$$

where $\otimes$ is the dyadic operator, the $\underline{e}_i$ are the basis vectors of the coordinate system and indices are $i = 1, 2, 3$ in three dimensions. To find

$$curl[F] = \underline{\nabla} \times [F] \tag{A2}$$

write the differential operator in the form

$$\underline{\nabla} = \sum_k \underline{e}_k \frac{\partial}{\partial x_k} \tag{A3}$$

such that

$$curl[F] = \sum_i \sum_j \sum_k \underline{e}_k \times \frac{\partial (F_{ij} \underline{e}_i \otimes \underline{e}_j)}{\partial x_k} \tag{A4}$$

For rectangular coordinates (x, y, z) the result is well known. The basis vectors are constant

$$\underline{e}_x = [1, 0, 0] \; \underline{e}_y = [0, 1, 0] \; \underline{e}_z = [0, 0, 1] \tag{A5}$$

and the differential operator is

$$\underline{\nabla} = \underline{e}_x \frac{\partial}{\partial x} + \underline{e}_y \frac{\partial}{\partial y} + \underline{e}_z \frac{\partial}{\partial z} \tag{A6}$$

so (A4) can be written as

$$curl[F] = \sum_i \sum_j \sum_k F_{ij,k}\ \underline{e}_k \times \left(\underline{e}_i \otimes \underline{e}_j\right) \tag{A7}$$

Using the relation

$$\underline{e}_i \times \left(\underline{e}_j \otimes \underline{e}_k\right) = (\underline{e}_i \times \underline{e}_k) \otimes \underline{e}_j \tag{A8}$$

we have

$$curl[F] = \sum_i \sum_j \sum_k F_{ij,k}\left(\underline{e}_k \times \underline{e}_j\right) \otimes \underline{e}_i \tag{A9}$$

and, as the basis is a set of orthogonal unit vectors,

$$\underline{e}_i \times \underline{e}_j = \epsilon_{ijk}\underline{e}_k \tag{A10}$$

where ε_{ijk} is the permutation tensor, we get

$$curl[F] = \sum_i \sum_j \sum_k F_{ij,k}\epsilon_{kjp}\underline{e}_p \otimes \underline{e}_i \tag{A11}$$

The result for rectangular coordinates is therefore

$$curl[F] = \begin{bmatrix} F_{xz,y} - F_{xy,z} & F_{yz,y} - F_{yy,z} & F_{zy,z} - F_{zz,y} \\ F_{xx,z} - F_{xz,x} & F_{yx,z} - F_{yz,x} & F_{zx,z} - F_{zz,x} \\ F_{xy,x} - F_{xx,y} & F_{yy,x} - F_{yx,y} & F_{zy,x} - F_{zx,y} \end{bmatrix} \tag{A12}$$

The result for cylindrical coordinates (r, θ, z) can be found by following the process, although the basis vectors are now not constant

$$\underline{e}_r = [\cos\theta, \sin\theta, 0]\ \underline{e}_\theta = [-\sin\theta, \cos\theta, 0]\ \underline{e}_z = [0, 0, 1] \tag{A13}$$

such that

$$\frac{\partial \underline{e}_r}{\partial \theta} = \underline{e}_\theta\ \frac{\partial \underline{e}_\theta}{\partial \theta} = -\underline{e}_r \tag{A14}$$

and the differential operator is given by

$$\underline{\nabla} = \underline{e}_r \frac{\partial}{\partial r} + \underline{e}_\theta \frac{1}{r}\frac{\partial}{\partial \theta} + \underline{e}_z \frac{\partial}{\partial z} \tag{A15}$$

Eq. (A4) can now be expanded to

$$\begin{aligned} curl[F] = &\sum_i \sum_j \sum_k F_{ij,k}\underline{e}_k \times \left(\underline{e}_i \otimes \underline{e}_j\right) + \underline{e}_\theta \\ &\times \frac{1}{r}[F_{rr}(\underline{e}_\theta \otimes \underline{e}_r + \underline{e}_r \otimes \underline{e}_\theta) + F_{r\theta}(\underline{e}_\theta \otimes \underline{e}_\theta - \underline{e}_r \otimes \underline{e}_r) \\ &+ F_{\theta r}(\underline{e}_\theta \otimes \underline{e}_\theta - \underline{e}_r \otimes \underline{e}_r) - F_{\theta\theta}(\underline{e}_r \otimes \underline{e}_\theta + \underline{e}_\theta \otimes \underline{e}_r) \\ &+ F_{rz}\underline{e}_\theta \otimes \underline{e}_z - F_{\theta z}\underline{e}_r \otimes \underline{e}_z + F_{zr}\underline{e}_z \otimes \underline{e}_\theta - F_{z\theta}\underline{e}_z \otimes \underline{e}_r] \end{aligned} \tag{A16}$$

The first term is the same (A7). Expanding out the cross-products in the second terms gives

$$\begin{aligned} curl[F] = &\sum_i \sum_j \sum_k F_{ij,k}\epsilon_{kjp}\underline{e}_p \otimes \underline{e}_i \\ &+ \frac{1}{r}[(F_{\theta\theta} - F_{rr})\underline{e}_z \otimes \underline{e}_\theta + (F_{\theta r} - F_{r\theta})\underline{e}_z \otimes \underline{e}_r \\ &+ F_{rz}\underline{e}_r \otimes \underline{e}_\theta - F_{\theta z}\underline{e}_r \otimes \underline{e}_r + F_{z\theta}\underline{e}_z \otimes \underline{e}_r] \end{aligned} \tag{A17}$$

or

$$curl[F] = \begin{bmatrix} F_{rz,\theta} - F_{r\theta,z} - \frac{F_{\theta z}}{r} & F_{\theta z,\theta} - F_{\theta\theta,z} + \frac{F_{rz}}{r} & F_{z\theta,z} - F_{zz,\theta} \\ F_{rr,z} - F_{rz,r} & F_{\theta r,z} - F_{\theta z,r} & F_{zr,z} - F_{zz,r} \\ F_{r\theta,r} - F_{rr,\theta} + \frac{F_{\theta r} - F_{r\theta}}{r} & F_{\theta\theta,r} - F_{\theta r,\theta} + \frac{F_{\theta\theta} - F_{rr}}{r} & F_{z\theta,r} - F_{zr,\theta} + \frac{F_{z\theta}}{r} \end{bmatrix} \tag{A18}$$

For the axisymmetric case of interest in this paper this reduces to

$$curl[F] = \begin{bmatrix} 0 & -F_{\theta\theta,z} + \frac{F_{rz}}{r} & 0 \\ F_{rr,z} - F_{rz,r} & 0 & F_{zr,z} - F_{zz,r} \\ 0 & F_{\theta\theta,r} + \frac{F_{\theta\theta} - F_{rr}}{r} & 0 \end{bmatrix} \tag{A19}$$

References

Calladine, C.R., 1985. Plasticity For Engineers: Theory and Applications. Elsevier.
Campbell, C.J., Gill, S.P.A., 2019. In Preparation.
Cao, D.M., Meng, W.J., Kelly, K.W., 2004. High-temperature instrumented microscale compression molding of Pb. Microsyst. Technol. 10, 323–328.
Chen, K., Meng, W.J., Mei, F., Hiller, J., Miller, D.J., 2010. From micro- to nano-scale molding of metals: size effect during molding of single crystal Al with rectangular strip punches. Acta Mater. 59, 1112–1120.
Cho, H.S., Hemker, K.J., Lian, K., Goettert, J., Dirras, G., 2003. Measured mechanical properties of LIGA Ni structures. Sens. Actuators A: Phys. 103, 59–63.
Ciavarella, M., Hills, D.A., Monno, G., 1998. The influence of rounded edges on indentation by a flat punch. Proc. Inst. Mech. Eng. Part C 212, 319–327.
De Guzman, M.S., Neubauer, G., Flinn, P., Nix, W.D., 1993. The role of indentation depth on the measured hardness of materials. In: MRS Online Proceedings Library Archive, p. 308.
Evans, A.G., Hutchinson, J.W., 2009. A critical assessment of theories of strain gradient plasticity. Acta Mater. 57, 1675–1688.
Fleck, N., Hutchinson, J., 1997. Strain gradient plasticity. Adv. Appl. Mech. 33, 296–361.
Gao, H., Huang, Y., Nix, W.D., Hutchinson, J.W., 1999. Mechanism-based strain gradient plasticity– I. Theory. J. Mech. Phys. Solids 47, 1239–1263.
Garofalo, F., 1965. Fundamentals of Creep and Creep-Rupture in Metals. McMillan Series in Materials Science.
Gourgiotis, P.A., Zisis, T., Baxevanakis, K.P., 2016. Analysis of the tilted flat punch in couple-stress elasticity. Int. J. Solids Struct. 85-86, 34–43.
Guha, S., Sangal, S., Basu, S., 2014. Numerical investigations of flat punch molding using a higher order strain gradient plasticity theory. Int. J. Mater. Forming 7, 459–467.
Gurtin, M.E., 2000. On the plasticity of single crystals: free energy, microforces, plastic-strain gradients. J. Mech. Phys. Solids 48, 989–1036.
Gurtin, M.E., 2002. A gradient theory of single-crystal viscoplasticity that accounts for geometrically necessary dislocations. J. Mech. Phys. Solids 50, 5–32.
Huang, Y., Zhang, F., Hwang, K.C., Nix, W.D., Pharr, G.M., Feng, G., 2006. A model of size effects in nano-indentation. J. Mech. Phys. Solids 54, 1668–1686.
Jiang, J., Meng, W.J., Sinclair, G.B., Lara-Curzio, E., 2006. Further experiments and modeling for microscale compression molding of metals at elevated temperatures. J. Mater. Res. 22, 1839–1848.
Johnson, K.L., 1987. Contact Mechanics. Cambridge University Press.
Kiener, D., Durst, K., Rester, M., Minor, A.M., 2009. Revealing deformation mechanisms with nanoindentation. JOM 61, 14.
Lu, B., Meng, W.J., 2014. Roll molding of microchannel arrays on Al and Cu sheet metals: a method for high-throughput manufacturing. J. Micro Nano-Manuf. 2, 011007–011009.
Ma, Q., Clarke, D.R., 1994. Size dependent hardness of silver single crystals. J. Mater. Res. 10, 853–863.
Meng, W.J., Cao, D.M., Sinclair, G.B., 2004. Stresses during micromolding of metals at elevated temperatures: pilot experiments and a simple model. J. Mater. Res. 20, 161–175.
Nielsen, K.L., Niordson, C.F., Hutchinson, J.W., 2014. Strain gradient effects in periodic flat punch indenting at small scales. Int. J. Solids Struct. 51, 3549–3556.
Nix, W.D., Gao, H., 1998. Indentation size effects in crystalline materials: a law for strain gradient plasticity. J. Mech. Phys. Solids 46, 411–425.
Oliver, W.C., Pharr, G.M., 1992. An improved technique for determining hardness and elastic modulus using load and displacement sensing indentation experiments. J. Mater. Res. 7, 1564–1583.
Pelletier, C.G.N., Dekkers, E.C.A., Govaert, L.E., den Toonder, J.M.J., Meijer, H.E.H., 2007. The influence of indenter-surface misalignment on the results of instrumented indentation tests. Polym. Test. 26, 949–959.
Pharr, G.M., Herbert, E.G., Gao, Y., 2010. The indentation size effect: a critical examination of experimental observations and mechanistic interpretations. Annu. Rev. Mater. Res. 40, 271–292.
Riccardi, B., Montanari, R., 2004. Indentation of metals by a flat-ended cylindrical punch. Mater. Sci. Eng. A 381, 281–291.
Shahjahan, N.B., Hu, Z., 2016. Effects of angular misalignment on material property characterization by nanoindentation with a cylindrical flat-tip indenter. J. Mater. Res. 32, 1456–1465.
Swadener, J.G., George, E.P., Pharr, G.M., 2002. The correlation of the indentation size effect measured with indenters of various shapes. J. Mech. Phys. Solids 50, 681–694.
Xu, Z.H., Li, X., 2007. Effect of sample tilt on nanoindentation behaviour of materials. Philos. Mag. 87, 2299–2312.